JOURNAL OF MATERIALS SCIENCE **36** (2001) 5143–5154

Microscopy and neutron diffraction study of a zirconium-8 wt% stainless steel alloy

D. P. ABRAHAM*, J. W. RICHARDSON JR., S. M. McDEAVITT
Argonne National Laboratory, 9700 S. Cass Ave., Argonne, IL 60439, USA
E-mail: abraham@cmt.anl.gov

The electrometallurgical treatment of zirconium-based and Zircaloy-clad spent nuclear fuels will yield a metal waste form. The baseline composition for the waste form is zirconium-8 wt% stainless steel (Zr-8SS). The microstructure of the Zr-8SS alloy has been studied by scanning electron microscopy, energy dispersive spectroscopy, and neutron diffraction. The phases present in the as-cast alloy include Zr(α), Zr_3(Fe,Ni), Zr_2(Fe,Ni), Zr_2(Fe,Cr), and Zr(Fe,Cr)$_2$; a solidification sequence has been proposed to explain the formation and morphology of these phases. Alloy phase stability has been studied by thermal aging at 780°C for periods up to 30 days. The phase changes that occur during thermal aging include an increase in Zr_3(Fe,Ni) and a decrease in Zr_2(Fe,Ni) content; reaction mechanisms have been proposed to explain these changes. The lattice parameters of alloy phases have been determined by neutron diffraction and found to be in agreement with those previously reported for similar phases. This study of alloy microstructures is the first step towards understanding the actinide and fission product distribution and predicting the corrosion behavior of the Zr-8SS metal waste form.

1. Introduction

Argonne National Laboratory (ANL) is developing an electrometallurgical process for the treatment of spent nuclear fuel [1]. The central feature of the process is electrorefining of the spent fuel in a molten salt electrolyte. Chopped segments of the spent fuel are placed into the anode baskets of an electrorefiner. When a potential is applied, components of the spent fuel dissolve at the anode, while uranium is deposited onto a steel cathode. At the end of the electrorefining operation, the fuel cladding, miscellaneous assembly hardware, noble metal fission products, and actinide elements remaining in the anode baskets are consolidated by melting into a metal waste form. This waste form must have sufficient corrosion resistance and mechanical integrity for eventual disposal in a geologic repository. The zirconium-8 wt% stainless steel alloy (Zr-8SS) has been developed as a baseline waste form for zirconium-based and Zircaloy-clad spent nuclear fuels [2].

The properties of an alloy are determined by its microstructural characteristics. For example, the general corrosion resistance of Zircaloy-2 in steam and hot water is substantially better than that of pure zirconium, even though the total concentration of alloying elements is less than 2% [3, 4]. The partition of iron, chromium, and nickel into intermetallic particles has a significant impact on the corrosion behavior of the alloy. In a similar manner, the repository performance of the Zr-8SS waste form will be governed by its microstructure. Hence, an understanding of alloy microstructure is crucial to predicting the corrosion resistance, mechanical behavior, and thermophysical properties of the waste form. Furthermore, knowledge of the Zr-8SS microstructure provides a basis for studying the noble metal and actinide distribution in the alloy.

This article presents results of neutron diffraction measurements and scanning electron microscopy on Zr-8SS (SS304-92 wt% Zr). Microstructural examination showed that the observed phases are similar to those in Zircaloy-2, even though the amounts of Fe, Cr, and Ni are much larger in the Zr-8SS alloy. The measured lattice parameters are also comparable to values reported for similar phases in Zircaloys and other zirconium-rich alloys. Since phase stability is an important criterion for waste form alloys, the effect of thermal aging on phase compositions and stability is also discussed in this article.

2. Experimental

2.1. Alloy preparation and chemical analysis

Ingots of Zr-8SS alloy weighing ~2.5 kg were prepared in an induction casting furnace attached to a controlled-atmosphere glovebox. High-purity zirconium and stainless steel rods were contained in a 10-cm (4-in.) diameter yttrium oxide crucible; this crucible was placed within a graphite susceptor that was heated by the induction field. The materials were alloyed at 1600°C under high-purity argon for ~1 h; the melt was furnace-cooled to obtain the solidified ingots.

*Author to whom all correspondence should be addressed.

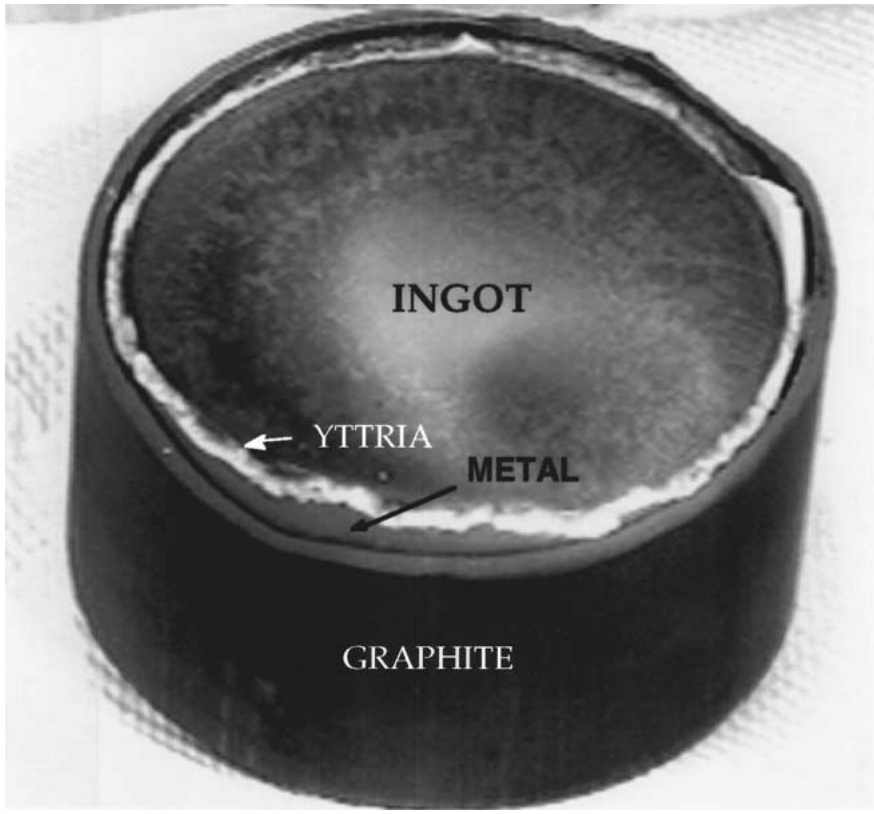

Figure 1 Photograph showing an as-cast Zr-8SS ingot bonded to the yttrium oxide crucible.

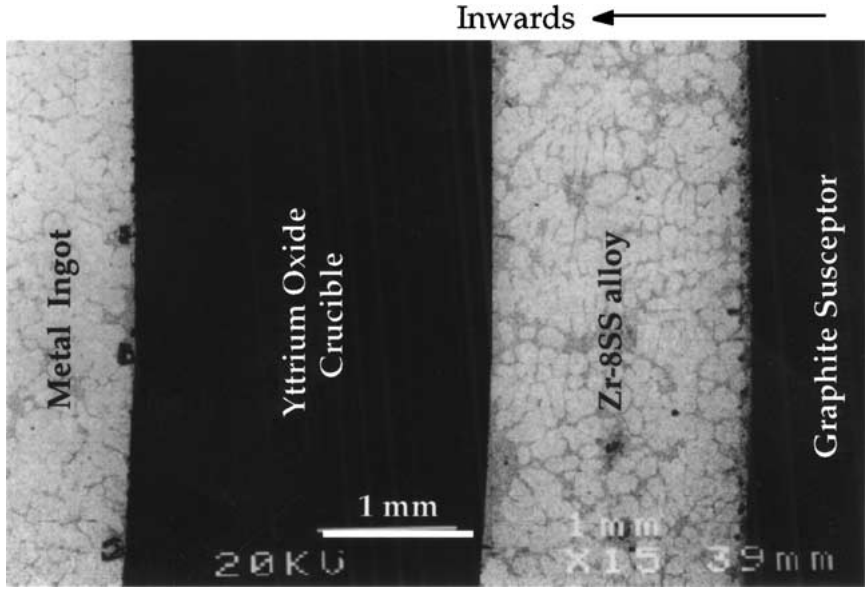

Figure 2 Back-scattered micrograph of as-cast Zr-8SS ingot showing an outer graphite layer, an intermediate metallic layer, the yttrium oxide crucible, and the metal ingot.

The yttrium oxide crucible cracked during processing, and metal filled the space between the crucible and the graphite susceptor. A photograph of the as-cast ingot bonded to the yttrium oxide crucible and graphite susceptor is shown in Fig. 1. The back-scattered image in Fig. 2 clearly shows the outer graphite layer, a metallic layer between the graphite and the melt crucible, the yttrium oxide crucible, and the Zr-8SS alloy. The ingot top surfaces were slag-free and showed a metallic luster. Slag formation may have been prevented by the significant solubility of zirconium for impurities from the furnace environment, such as carbon, nitrogen, and oxygen.

Specimens for microscopy, neutron diffraction, and chemical analyses were obtained from the ingot interior to minimize contamination from the crucible. However, yttrium oxide pieces were occasionally found dispersed in the alloy microstructure. Chemical analyses of specimens from sections of the ingot also showed the presence of yttrium. A typical composition of a Zr-8SS alloy ingot is shown in Table I. It is evident that Fe, Cr, Ni, and Zr are the major elements in the alloy. The small

TABLE I Typical composition of Zr-8SS alloy (wt%)[a]

	Fe	Cr	Ni	Zr	Mn	Mo	Co	Cu	Sn	Y	C
Zr-8SS	5.1	1.4	0.6	91.9	0.12	0.03	0.01	0.03	0.07	0.22	0.017

[a]Determined by inductively coupled plasma emission spectroscopy. Estimated accuracy is $\sim \pm 5\%$.

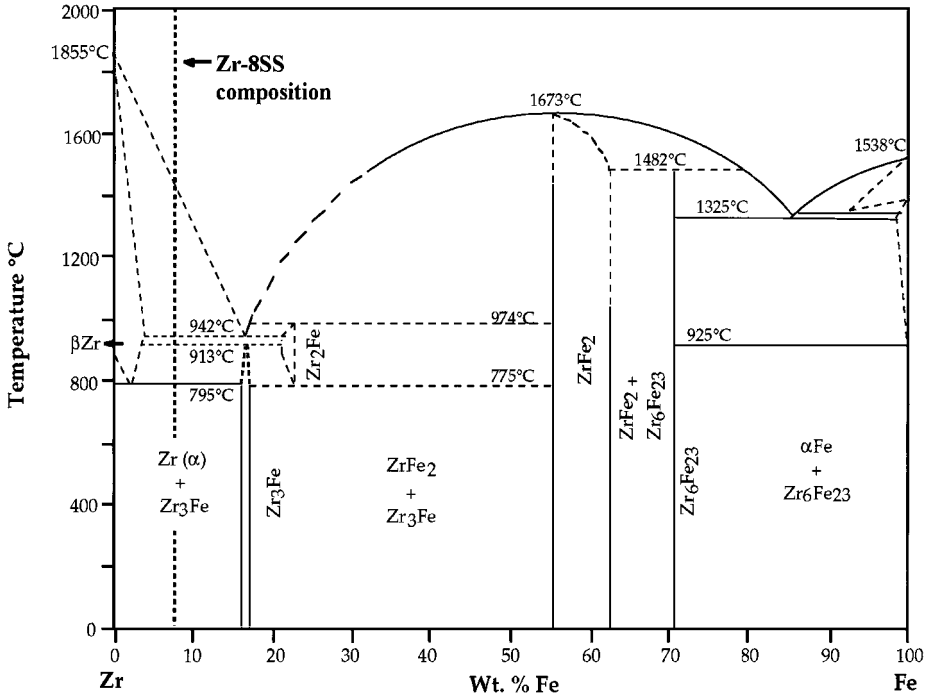

Figure 3 The Fe-Zr binary phase diagram, based on Arias *et al.* [5].

amounts of Mo, Co, Cu, and Sn did not have a significant effect on alloy microstructure and are hence not included in further discussions.

Samples from an as-cast Zr-8SS alloy ingot were thermally aged at 780°C for time periods up to 30 days to accelerate phase changes that occur below the Zr(α)-to-Zr(β) transition temperature. The samples were contained in quartz crucibles that were evacuated and back-filled with argon gas. The selection of the aging temperature was based on a recent Fe-Zr phase diagram (Fig. 3) presented by Arias *et al.* [5], which indicates that the Zr(α)-to-Zr(β) transition temperature is at 795°C. Older versions of the phase diagram [6] indicated a lower transition temperature (~730°C). However, recent thermal property measurements on Zr-8SS alloy samples have confirmed the higher transition temperature [7].

2.2. Microscopy and neutron diffraction

Alloy samples were examined by a JEOL 6400 scanning electron microscope (SEM) operating in both secondary electron and back-scattered electron modes. Standardless quantitative analysis of individual phases was obtained with an energy dispersive spectrometer (EDS) and Vantage software from NORAN instruments. The uncertainty in elemental compositions determined by this method is $\sim \pm 3\%$ of the measured value.

Time-of-flight neutron diffraction data were collected from as-cast and thermally aged samples on the General Purpose Powder Diffractometer at the Intense Pulsed Neutron Source, ANL. These experiments are carried out at a fixed scattering angle, and diffraction patterns were generated as a function of incident neutron wavelength. Diffraction data were collected at six separate data banks, each positioned at a fixed 2θ angle relative to the incident beam. Each detector bank accessed a limited range of d-spacings, defined by the available wavelength range. Ranges for the banks used in this study are $2\theta = \pm 148^\circ$, $d \sim 0.05$–0.3 nm; $2\theta = \pm 90^\circ$, $d \sim 0.07$–0.4 nm; and $2\theta = \pm 60^\circ$, $d \sim 0.08$–0.54 nm. Rietveld refinements [8] were conducted on the neutron diffraction data to obtain phase contents and lattice parameters in the alloy samples.

For many applications, such as those without reflections with d-spacings higher than 0.3 nm, refinement of back-scattered neutron data ($2\theta = \pm 148^\circ$) is sufficient for phase analysis. Combined analysis of the six data banks was chosen in our experiments for three reasons. First, slight variations in refined lattice parameters for the different banks were used to calculate minor corrections ($\Delta a/a \leq 2 \times 10^{-4}$) caused by possible offsets in the centroid of scattering from the center of the instrument. Second, the preferred orientation (sample texture) could be assessed from bank-to-bank intensity variations since each detector bank viewed the sample from a different orientation. Third, phase contents could be estimated by averaging results from all detector banks, hence reducing the influence of texture.

TABLE II Phase content estimates and lattice parameters in as-cast and thermally-aged Zr-8SS alloys determined by neutron diffraction

Zr-8SS Ingot	Phase	Content, vol%	Lattice Parameters, nm		
			a	*b*	*c*
As-Cast	Zr(α)	76.2 ± 1.6	0.3231	–	0.5151
	Zr_3Fe-type	3.6 ± 0.6	0.3320	1.1020	0.8821
	Zr_2Fe-type 1	10.3 ± 1.1	0.6439	–	0.5450
	Zr_2Fe-type 2	0.5 ± 0.4	0.6473	–	0.5468
	$ZrFe_2$-type	9.4 ± 1.1	0.5032	–	0.8239
Aged	Zr(α)	75.2 ± 0.9	0.3234	–	0.5155
780°C, 30 d	Zr_3Fe-type	12.3 ± 0.2	0.3326	1.0973	0.8829
	Zr_2Fe-type 1	4.3 ± 0.6	0.6461	–	0.5435
	Zr_2Fe-type 2	0	–	–	–
	$ZrFe_2$-type	8.3 ± 0.6	0.5034	–	0.8244

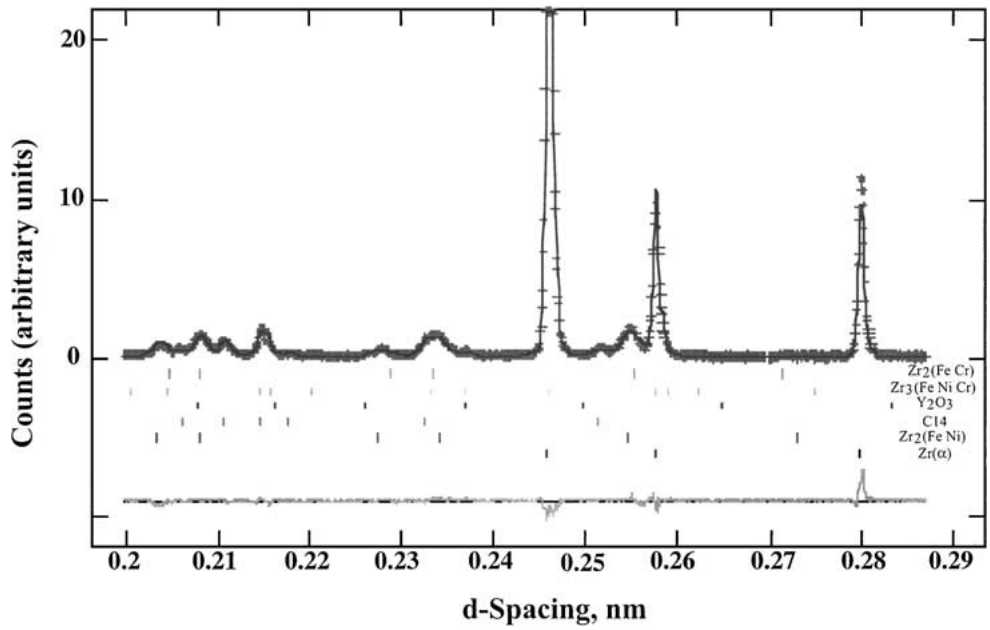

Figure 4 Rietveld profile plot for as-cast Zr-8SS alloy. Observed counts are identified with "+" marks, while the calculated spectrum is represented by the solid curve. Plotted at the bottom is the difference between observed and calculated data. Vertical bars identify expected locations of diffraction peaks for the respective phases.

3. Results

3.1. Neutron diffraction analysis

The neutron diffraction pattern obtained from as-cast Zr-8SS alloy showed peaks corresponding to Zr(α), a Zr_3Fe-type intermetallic, two Zr_2Fe-type intermetallics, and a $ZrFe_2$-type C14 Laves intermetallic; a portion of the diffraction pattern is shown in Fig. 4. A slight peak broadening was observed for the Zr_3Fe-type intermetallic, which indicated the possible presence of small amounts of a related phase. Observable imperfections in the fit to the Zr(α) phase intensity data were either the result of preferred orientation (crystallographic texture) or due to scattering contributions from interstitial species, such as oxygen. The intermetallic phases showed considerable crystallographic texture; this is not readily apparent in Fig. 4 because of the dominance of the Zr(α) phase. The texture observed in the phases apparently resulted from the casting process and persisted even after the 780°C thermal aging.

Table II lists the phase content estimates and lattice parameters calculated from Rietveld refinements. The primary phase in the alloy was Zr(α). The alloy also contained ~10.3 vol% of the Zr_2Fe-type 1 phase, ~0.5 vol% of the Zr_2Fe-type 2 phase, ~9.4 vol% of the $ZrFe_2$-type phase, and ~3.6 vol% of the Zr_3Fe-type intermetallic. Minor yttrium oxide peaks observed in the diffraction patterns were from the melt-crucible material, and data on phase content are not included in Table II.

Fig. 5 is a portion of the neutron diffraction pattern obtained from a Zr-8SS alloy that was thermally aged at 780°C for 30 days. The plot shows a dramatic increase in the intensity of the Zr_3Fe-type peak (marked by arrow) and the disappearance of the Zr_2Fe-type 2 peak. Table II lists the phase content and lattice parameters in the thermally aged alloy; note the absence of the Zr_2Fe-type 2 phase.

The phase content change and the percentage change in lattice parameters induced by the thermal aging are given in Table III. An increase in phase content (+8.7 vol%) was observed for the Zr_3Fe-type phase. The amount of the Zr_2Fe-type 1 phase was smaller (−6.0 vol%) in the aged alloy. A small decrease in Zr(α) and $ZrFe_2$-type phase content is also seen in Table III; however, Table II indicates that these changes were within the range of experimental uncertainty.

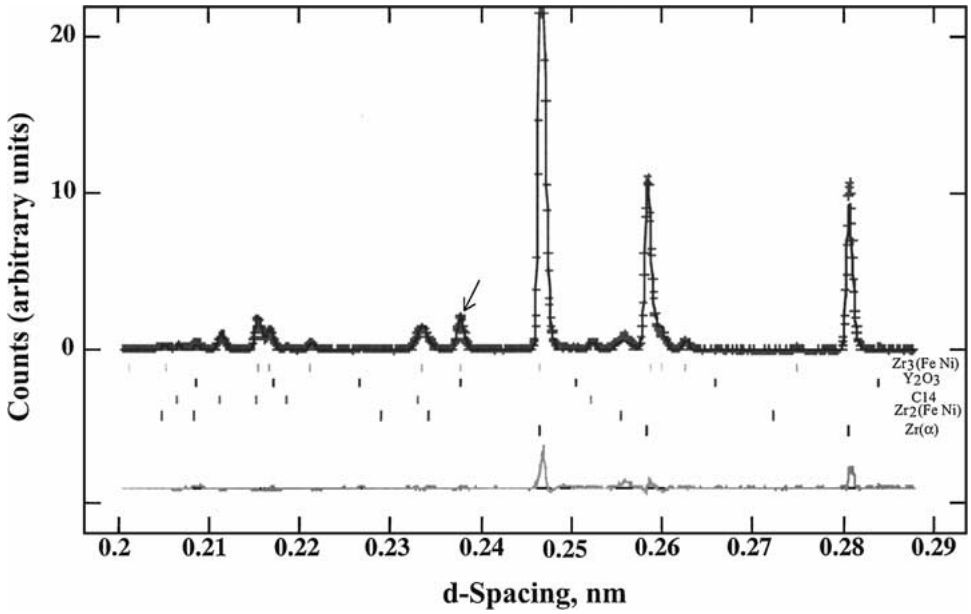

Figure 5 Rietveld profile plot for Zr-8SS alloy that was aged at 780°C for 30 days, showing dramatic increase in contribution from $Zr_3(Fe,Ni)$ (marked by arrow) and disappearance of $Zr_2(Fe,Cr)$.

Table III shows that the lattice parameters of the various phases were also affected by the thermal aging. A small increase in the *a* and *c* parameters of the Zr(α) phase was observed; this increase may be due to oxygen dissolution that could have occurred during aging. The Zr(α) phase is known to have considerable oxygen solubility [9]. Calculations based on Zr-O solid solution data [10] indicate that the atomic concentration of oxygen would have to be 2% higher in the aged than in the as-cast alloy to account for the observed lattice parameter changes. Small amounts of oxygen could have been present during thermal aging even though the quartz crucibles were evacuated and back-filled with Ar gas.

The lattice parameters for the $ZrFe_2$-type intermetallic were also slightly larger in the aged alloy. An increase in the a parameter and decrease in the c parameter was observed for the Zr_2Fe-type 1 phase. For the Zr_3Fe-type intermetallic, the thermal aging resulted in an increase of a and c parameters and a decrease in the b parameter. These lattice parameter changes may be attributed to the thermal relief of interphase stresses present in the as-cast alloy.

TABLE III Changes in phase content and lattice parameters measured in a Zr-8SS alloy after aging at 780°C for 30 days

Phase	Content change, vol %	Δa, %	Δb, %	Δc, %
Zr(α)	−1.0	0.080		0.085
Zr_3Fe-type	+8.7	0.19	−0.42	0.088
Zr_2Fe-type 1	−6.0	0.35		−0.27
Zr_2Fe-type 2	−0.5	–		–
$ZrFe_2$-type	−1.1	0.032		0.057

3.2. Microstructural analysis

Back-scattered micrographs obtained from as-cast Zr-8SS alloy samples are shown in Figs 6 to 11. Table IV lists the average phase compositions determined by point-to-point EDS analyses. Phases in the microstructure were identified by correlating the EDS data with the neutron diffraction results. The low-magnification image in Fig. 6 shows primary Zr(α) features; the "light" and "gray" contrasts observed in this micrograph are due to small variations in elemental compositions

TABLE IV Composition (at.%) of phases in Zr-8SS alloys determined by SEM/EDS

Ingot	Fe	Cr	Ni	Zr	Mn	Phase[a]	ND label[b]
As-Cast	0.9	0.2	0.4	97	0.3	Zr(α)-light	Zr(α)
	0.9	0.7	0.1	96	0.7	Zr(α)-gray	Zr(α)
	18.7	0.7	4.5	75	0.1	$Zr_3(Fe_{0.81}Ni_{0.19})$	Zr_3Fe-type
	15	8	0.7	75	0.5	$Zr_3(Fe_{0.65}Cr_{0.35})$	Zr_3Fe-type
	26.3	0.5	5.2	67	0.4	$Zr_2(Fe_{0.83}Ni_{0.17})$	Zr_2Fe-type 1
	20	11	0.7	66.3	0.8	$Zr_2(Fe_{0.65}Cr_{0.35})$	Zr_2Fe-type 2
	38	22.3	0.8	36.6	2	$Zr_{1.09}(Fe_{0.61}Cr_{0.36}Mn_{0.03})_{1.91}$	$ZrFe_2$-type
Aged	0.3	0.2	0.2	97	0.2	Zr(α)-light	Zr(α)
780°C, 30 d	0.3	0.3	0.6	97	0.2	Zr(α)-gray	Zr(α)
	20	0.2	4	75	0.1	$Zr_3(Fe_{0.83}Ni_{0.17})$	Zr_3Fe-type
	25.1	0.7	5.3	68.4	0.5	$Zr_2(Fe_{0.83}Ni_{0.17})$	Zr_2Fe-type 1
	40	23.2	0.5	34	2	$Zr_{1.02}(Fe_{0.61}Cr_{0.36}Mn_{0.03})_{1.98}$	$ZrFe_2$-type

[a]Only major elements are included in this designation.
[b]From neutron diffraction analyses (see Tables II and III).

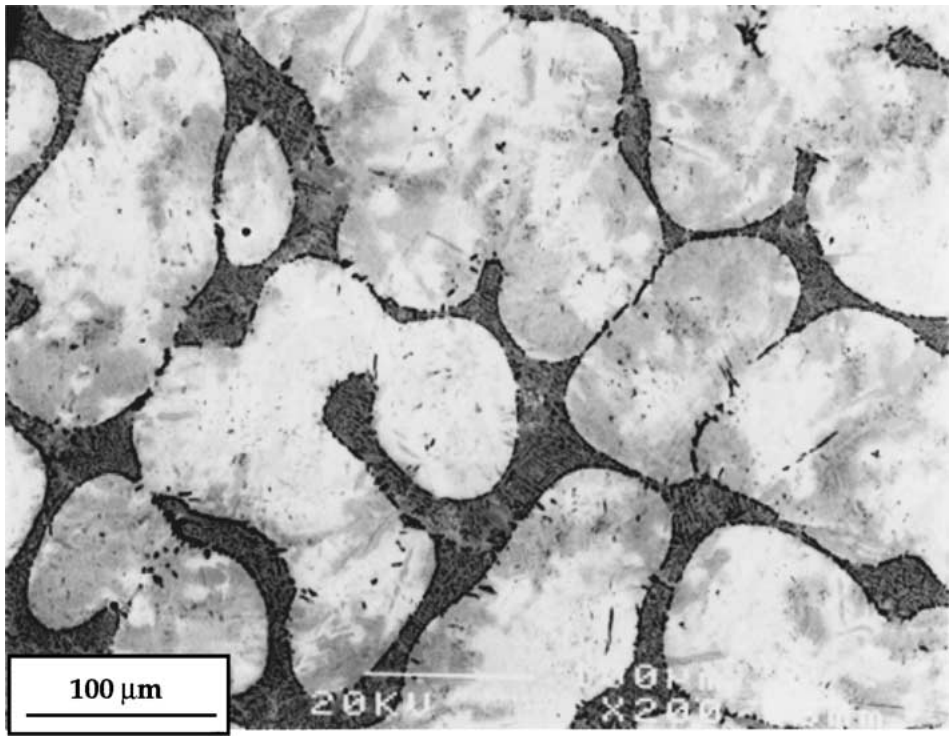

Figure 6 Low-magnification micrograph of as-cast Zr-8SS alloy. Observe the "light" and "gray" contrasts within the primary Zr(α) features.

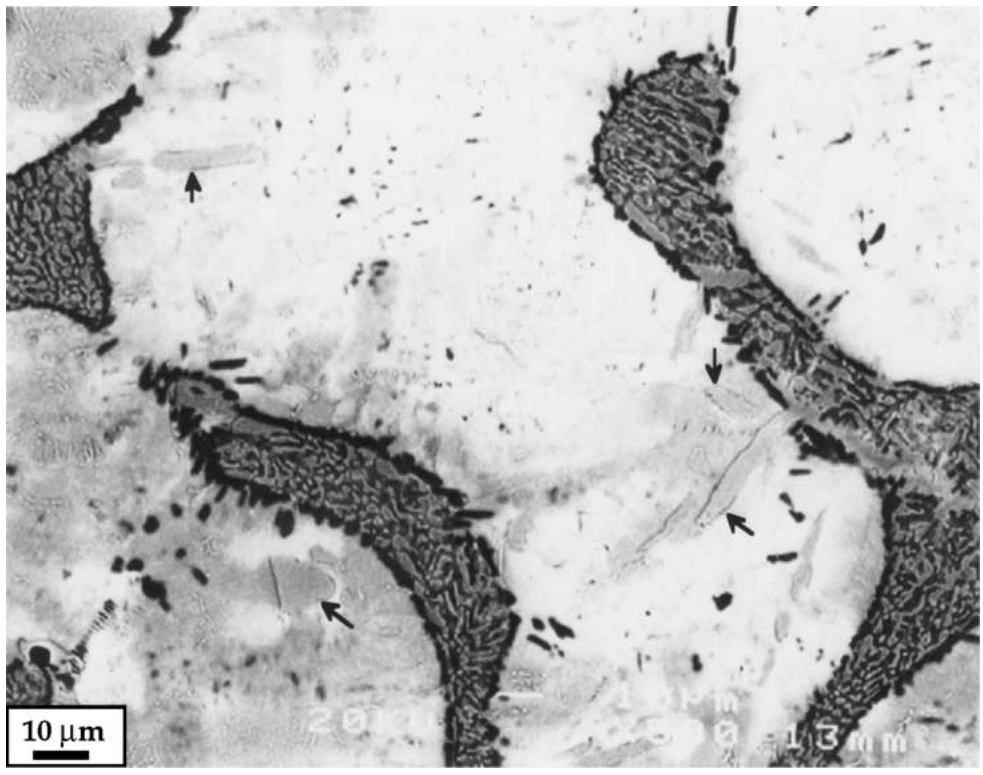

Figure 7 Micrograph from as-cast Zr-8SS alloy showing Zr_3(Fe,Ni) features (marked by arrows) within the primary Zr(α) features. The dark ring that borders the Zr(α) features is a $ZrFe_2$-type Laves intermetallic.

within the phase. Lath-like structures, commonly reported by investigators studying Zircaloy microstructures, were not observed in the primary Zr(α).

A Zr_3Fe-type intermetallic is observed within the primary Zr(α); this phase also contains Ni (see Table IV) and is labeled $Zr_3(Fe_{0.81}Ni_{0.19})$. The distinct morphologies of this phase are shown in Figs 7 and 8. The dark ring that borders the primary Zr(α) features (see Figs 6 to 8) is a $ZrFe_2$-type Laves intermetallic. As given in Table IV, the phase contains ~36 at.% Zr, which is greater than the stoichiometric zirconium content (33.3 at.%). The phase also contains Cr and Mn and has been labeled $Zr_{1.09}(Fe_{0.61}Cr_{0.36}Mn_{0.03})_{1.91}$ in the table. Small amounts of this intermetallic are also observed within the primary Zr(α). In some areas of the sample, the Zr(α) features are only sparsely bounded by the Laves

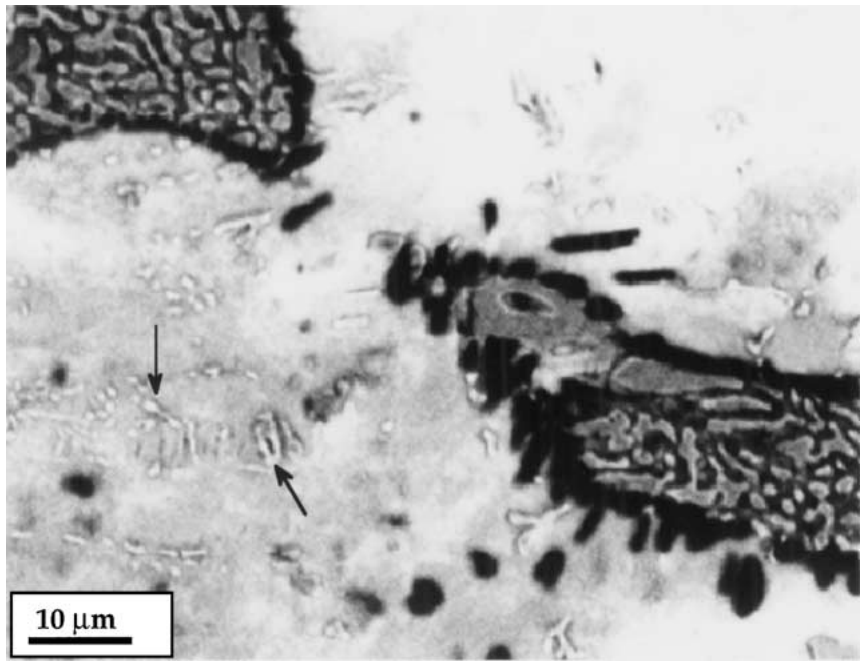

Figure 8 Back-scattered micrograph of as-cast Zr-8SS alloy showing $Zr_3(Fe,Ni)$ features (marked by arrows) within the primary Zr(α). The dark ring that borders Zr(α) is a $Zr(Fe,Cr)_2$ Laves intermetallic.

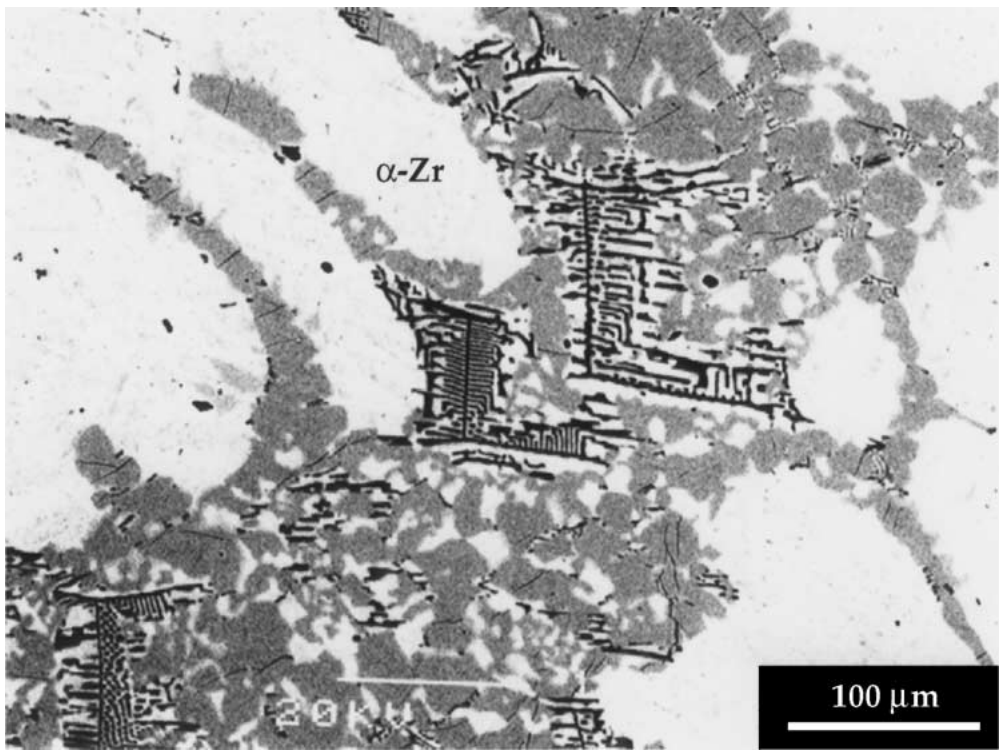

Figure 9 Back-scattered micrograph showing eutectic structures between the primary Zr(α) features. The eutectics are a mixture of Zr(α) and $Zr(Fe,Cr)_2$ phases.

intermetallic. Instead, the intermetallic appears within a eutectic morphology along with the Zr(α) phase (see Figs 9 and 10).

The most-prominent phase in the region between the primary Zr(α) features (see Figs 9 and 11) is a Ni-bearing Zr_2Fe-type phase labeled $Zr_2(Fe_{0.83}Ni_{0.17})$ in Table IV. The other phases in this region include Zr(α) and the $ZrFe_2$-type Laves intermetallic. As shown in Table IV, also observed are small amounts of a Cr-bearing Zr_2Fe-type phase, labeled $Zr_2(Fe_{0.65}Cr_{0.35})$; a Cr-bearing Zr_3Fe-type phase, labeled $Zr_3(Fe_{0.65}Cr_{0.35})$; and $Zr_3(Fe_{0.81}Ni_{0.19})$. The slight peak broadening observed for the Zr_3Fe-type intermetallic in neutron diffraction patterns of the as-cast alloy is probably due to the presence of the two Zr_3Fe-type phases.

Figs 12 and 13 show that both microstructure and phase morphology are affected by the 780°C, 30-day aging; average elemental compositions for the phases are reported in Table IV. The changes in phase elemental composition induced by the thermal aging are generally

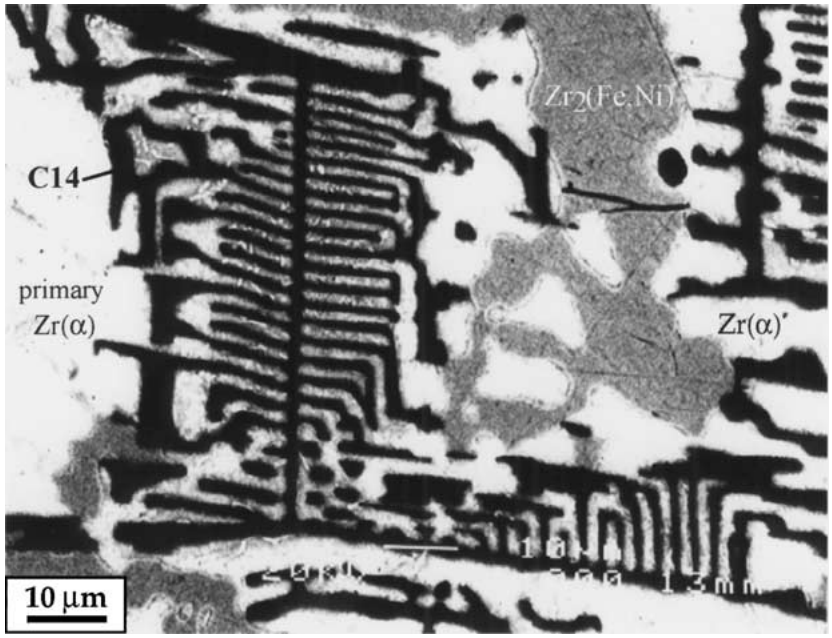

Figure 10 Magnified image of area in Fig. 9 showing eutectic structures containing Zr(α) and $Zr(Fe,Cr)_2$. The $Zr_2(Fe,Ni)$ intermetallic and a part of primary Zr(α) are also seen.

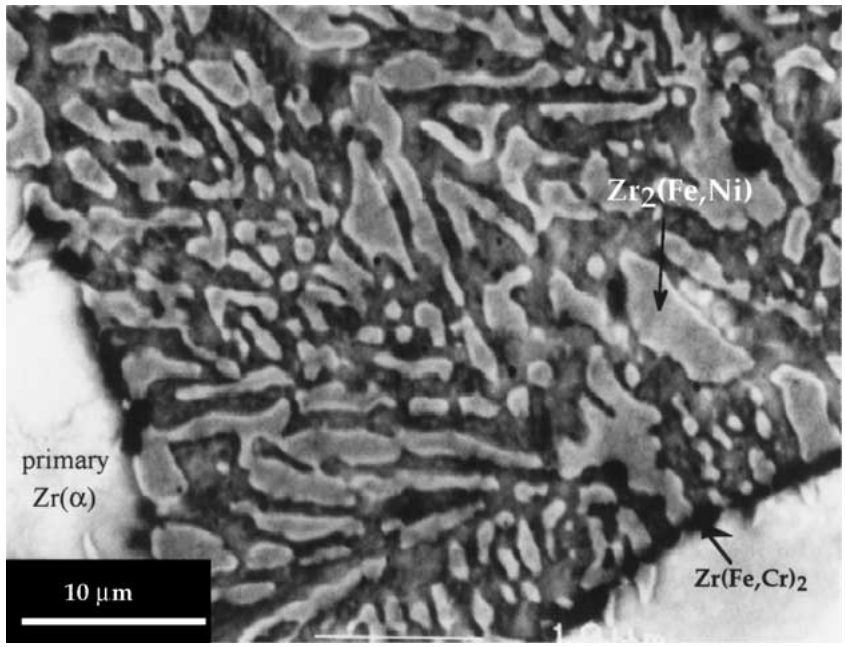

Figure 11 Back-scattered micrograph showing the $Zr_2(Fe,Ni)$ between the primary Zr(α) phase. The area around $Zr_2(Fe,Ni)$ contains a mixture of $Zr_2(Fe,Cr)$, $Zr_3(Fe,Ni)$, and $Zr_3(Fe,Cr)$ phases. The $Zr(Fe,Cr)_2$ intermetallic bordering primary Zr(α) is also observed.

small (see Table V) and mostly within the uncertainty of the EDS measurements. The $Zr_3(Fe_{0.65}Cr_{0.35})$ and $Zr_2(Fe_{0.65}Cr_{0.35})$ phases were not observed in the aged alloy, indicating that they are metastable in the as-cast alloy.

TABLE V Calculated changes in phase composition (at.%) in Zr-8SS alloy after aging at 780°C for 30 days

Phase	ΔFe	ΔCr	ΔNi	ΔZr	ΔMn
Zr(α)-light	−0.6	0	−0.2	0	−0.1
Zr(α)-gray	−0.6	−0.4	0.5	1	−0.5
$Zr_3(Fe_{0.83}\ Ni_{0.17})$	1.3	−0.5	−0.5	0	0
$Zr_2(Fe_{0.83}\ Ni_{0.17})$	−1.2	0.2	0.1	1.4	0.1
$Zr_{1.02}(Fe_{0.61}Cr_{0.36}\ Mn_{0.03})_{1.98}$	2	0.9	−0.3	−2.6	0

In Fig. 12, the $Zr_3(Fe,Ni)$ phase (marked by arrows) is clearly visible in the primary Zr(α) features. A comparison of Figs 11 and 13 shows that the $Zr_2(Fe,Ni)$ phase is not as distinct in the aged alloy. The area around $Zr_2(Fe,Ni)$ contains Zr(α), $Zr_3(Fe,Ni)$, and a relatively coarse $Zr(Fe,Cr)_2$ intermetallic. Coarsening of the $Zr(Fe,Cr)_2$ intermetallic was also observed within the primary Zr(α) phase (see Fig. 12).

4. Discussion

4.1. Phases observed in as-cast Zr-8SS alloy

The microstructural phases observed in as-cast Zr-8SS alloy may be deduced from an examination of the Fe-Zr binary [5], Fe-Cr-Zr ternary [11], and Fe-Ni-Zr

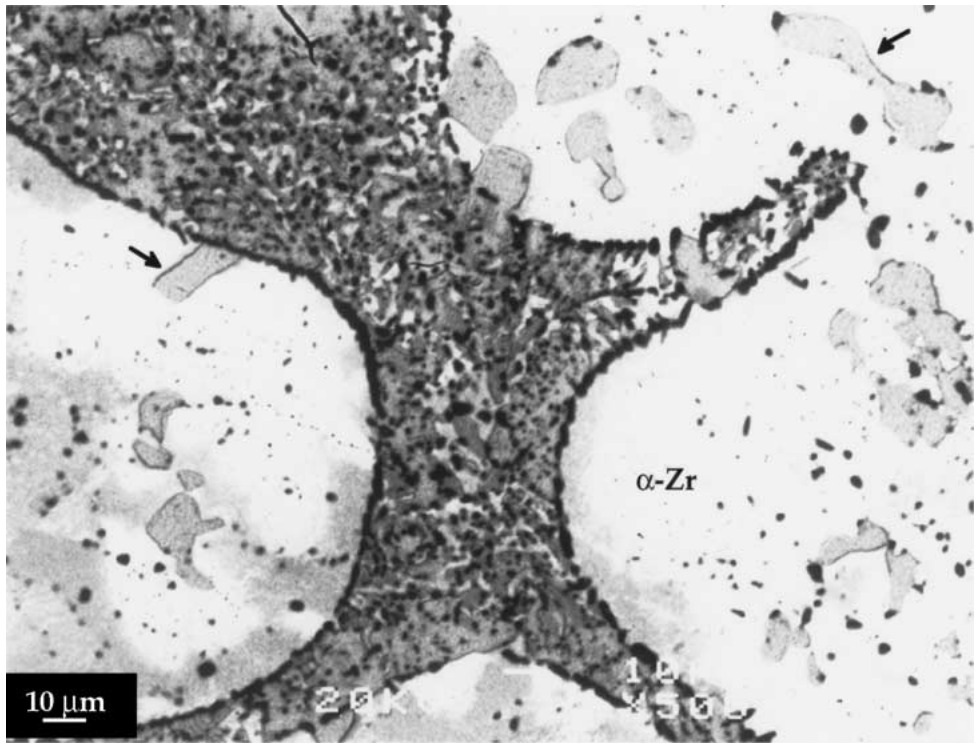

Figure 12 Micrograph of Zr-8SS alloy that was aged at 780°C for 30 days. The $Zr_3(Fe,Ni)$ intermetallic (marked by arrows) is distinctly visible within the primary Zr(α) features. The $Zr(Fe,Cr)_2$ Laves intermetallic, both within and between primary Zr(α), is coarser than in the as-cast alloy.

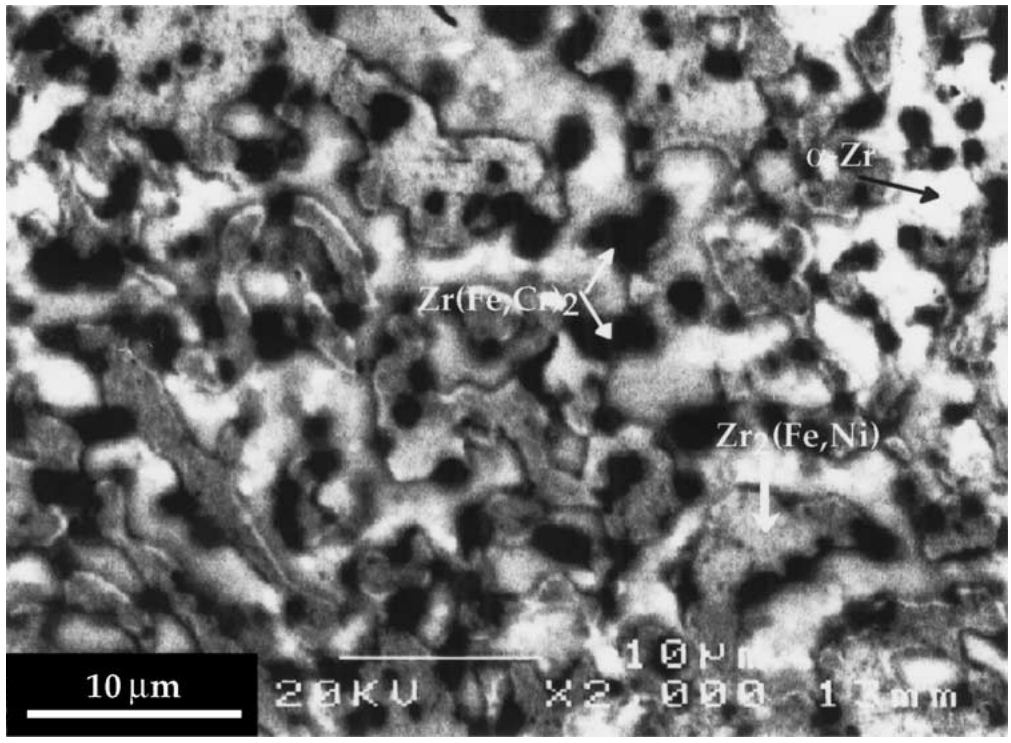

Figure 13 Higher magnification image showing the region between the primary Zr(α) features. The $Zr_2(Fe,Ni)$ phase is not as distinct as in Fig. 11; the area around it contains Zr(α), $Zr_3(Fe,Ni)$, and a relatively coarse $Zr(Fe,Cr)_2$ intermetallic.

ternary [12] phase diagrams. The proposed solidification sequence from the melt is presented in Table VI. At 1600°C, all constituents of the alloy are in the liquid state. The Zr(β) phase precipitates out of the liquid at ∼1480°C and increases in quantity as cooling proceeds. At ∼1020°C, the Fe-Cr-Zr ternary indicates that some of the liquid transforms into a eutectic mixture of Zr(β) and a $ZrFe_2$-type phase; the latter phase is probably $Zr(Fe,Cr)_2$ because $ZrFe_2$ and $ZrCr_2$ are mutually soluble and form a continuous series of solid solutions [11, 13–15]. The precipitation of the Fe- and Cr-rich phase results in a relative Ni-enrichment of the remaining liquid.

At ∼940°C, cooling continues with the precipitation of a Zr_2Fe-type phase. This phase is probably the $Zr_2(Fe,Ni)$-type because of the relative enrichment of

TABLE VI Proposed solidification sequence in the as-Cast Zr-8SS alloy[a]

Temperature	Alloy phases and proportion
~1600°C	Liquid
~1480°C	Liquid + Zr(β)
~1020°C	Liquid + Zr(β) + $Zr(Fe,Cr)_2$
~940°C	Zr(β) − major + $Zr(Fe,Cr)_2$ − minor + Zr_2(Fe,Ni) − minor + Zr_2(Fe,Cr) − v.v. minor
~910°C	Zr(β) − major + $Zr(Fe,Cr)_2$ − minor + Zr_2(Fe,Ni) − minor + Zr_2(Fe,Cr) − v.v. minor + Zr_3(Fe,Ni) − v.v. minor + Zr_3(Fe,Cr) − v.v.v. minor
<795°C	Zr(α) − major + $Zr(Fe,Cr)_2$ − minor + Zr_2(Fe,Ni) − minor + Zr_2(Fe,Cr) − v.v. minor + Zr_3(Fe,Ni) − v. minor + Zr_3(Fe,Cr) − v.v.v. minor

[a]Phase formation temperatures are approximate and based on data in the Fe-Zr phase diagram [5].

Ni in the solidifying liquid. Furthermore, Zr_2Fe and Zr_2Ni have the tetragonal Al_2Cu-type (C16) structure and form a continuous series of solid solutions at high temperatures [16]. A small quantity of non-equilibrium Zr_2(Fe,Cr) may have formed at this time; note that Zr_2Cr is not observed in the Cr-Zr phase diagram [17].

The $Zr(Fe,Cr)_2$ phase remains within the eutectic structures (Figs 9 and 10) or is confined to areas along the Zr(β)-Zr_2(Fe,Ni) phase boundaries. At ~913°C, the Fe-Zr phase diagram indicates that the Zr_2Fe-type phase will transform into a Zr_3Fe-type phase. Sawicki *et al*. studied the Zr_2Fe-Zr_3Fe peritectoid transformation in a single-crystal Zr-0.065 at.% Fe alloy and showed that Zr_3Fe formation is slow and limited by bulk diffusion [18]. In the Zr-8SS alloy, the Zr_2Fe-Zr_3Fe transformation is expected to be very slow; only a very small fraction of Zr_2(Fe,Ni) will transform into Zr_3(Fe,Ni) during cooling of the as-cast alloy. Moreover, the slow diffusion limits Zr_3(Fe,Ni) to the outer areas of the Zr_2(Fe,Ni) phase. A very small quantity of non-equilibrium Zr_3(Fe,Cr) may also have formed from Zr_2(Fe,Cr) during this process.

At ~795°C, Zr(β) transforms into Zr(α). Several authors have described this transformation in zirconium alloys with small amounts of alloying elements [19–23]. The Zr(β) phase transforms into Zr(α) by a martensitic or bainitic transformation; martensitic transformation occurs for cooling rates exceeding ~1500°C/s [24]. For lower cooling rates, lath-like Zr(α) nuclei originate from the Zr(β) grain boundary and extend towards the grain center. Betagenic elements (such as Fe, Cr, and Ni) diffuse from the α nuclei to the untransformed β phase. On solidification, the alloy microstructure contains colonies composed of parallel laths with the intermetallic precipitates localized at the lath boundaries.

Lath-like structures were not observed in the as-cast Zr-8SS alloy (see Figs 6–8, 11). Furthermore, the Fe, Cr, and Ni solute elements did not segregate to $\beta-\alpha$ boundaries, as commonly observed in Zircaloys. The diffusion process that led to the formation of Zr(α) appears to have resulted in the formation of relatively solute-rich regions (gray contrast) and solute-poor regions (light contrast) observed in the primary Zr(α) (see Figs 6 and 7). Some of the solute-rich regions underwent phase transformation, which explains the small amounts of Zr_3(Fe,Ni) and $Zr(Fe,Cr)_2$ observed within the primary Zr(α) features (Figs 7 and 8).

4.2. Phase changes on thermal aging

The phases in the aged Zr-8SS alloy are Zr(α), Zr_3(Fe,Ni), Zr_2(Fe,Ni), and the $Zr(Fe,Cr)_2$ intermetallic. The Zr_3(Fe,Cr) and Zr_2(Fe,Cr) phases are metastable and not present in the aged alloy. Tables II and III show that thermal aging results in a decrease of the Zr_2(Fe,Ni) phase and an increase in the amount of Zr_3(Fe,Ni). The micrographs of the aged alloy show that the amount of Zr_3(Fe,Ni) increases both between and within the primary Zr(α) features. The small decreases in the amount of Zr(α) and the $Zr(Fe,Cr)_2$ intermetallic are within the experimental uncertainty of the neutron diffraction measurements.

The following mechanisms may explain the phase changes observed during thermal aging. The metastable Zr_3(Fe,Cr) and Zr_2(Fe,Cr) phases, present between the primary Zr(α) features, transform into $Zr(Fe,Cr)_2$ according to:

$$Zr_3(Fe,Cr) = 0.5Zr(Fe,Cr)_2 + 2.5Zr(\alpha) \quad (1)$$

$$Zr_2(Fe,Cr) = 0.5Zr(Fe,Cr)_2 + 1.5Zr(\alpha) \quad (2)$$

Since the Zr_3(Fe,Cr) and Zr_2(Fe,Cr) content in the as-cast alloy is small, the amount of $Zr(Fe,Cr)_2$ generated during the transformations is very small and is not detected by the diffraction measurements. A relatively larger amount of Zr(α) is created during the transformations, which reacts with some of the Zr_2(Fe,Ni) to form Zr_3(Fe,Ni):

$$Zr_2(Fe,Ni) + Zr(\alpha) = Zr_3(Fe,Ni) \quad (3)$$

This may explain the observed decrease in Zr_2(Fe,Ni) content and the increase in Zr_3(Fe,Ni) content between the primary Zr(α) features.

Sawicki *et al*. [18] noted a strong barrier to the nucleation of Zr_3Fe within the Zr(α) matrix in a Zr-0.065 at.% Fe alloy. In the Zr-8SS alloy, however, the supersaturation of solute elements provides a strong driving force for Zr_3(Fe,Ni) formation, which could result in the observed increase within the primary Zr(α) matrix (see Fig. 12). The creation of Zr(α) during the decomposition of the Zr_3(Fe,Cr) and Zr_2(Fe,Cr) phases and the consumption of the phase during Zr_3(Fe,Ni) formation may result in the very small net decrease in Zr(α) content, shown in Tables II and III.

The thermal aging results in a coarsening of the $Zr(Fe,Cr)_2$ intermetallic (compare Figs 13 and 11). Bangaru (Rao) also reported a coarsening of intermetallic particles during high-temperature alpha-phase annealing of Zircaloy-4 [23]. The driving force for particle coarsening comes from the need to lower the interfacial energy [25] and reduce the solute supersaturation of Fe and Cr both within and between the primary Zr(α) features.

4.3. Comparison of lattice parameters

Table VII compares the lattice parameters measured in the aged Zr-8SS alloy with those of similar phases

TABLE VII Comparison of lattice parameters (nm) measured in Zr-8SS alloy (aged at 780°C, 30 days) with literature values

Phase in Zr-8SS Ingot	Measured	Literature	Comments [reference]
$Zr(\alpha)$	$a = 0.3234$ $c = 0.5155$	$a = 0.3233$ $c = 0.5149$	$Zr(\alpha)$ [26]
$Zr_3(Fe_{0.83}Ni_{0.17})$	$a = 0.3326$ $b = 1.0973$ $c = 0.8829$	$a = 0.332$ $b = 1.099$ $c = 0.881$	$Zr_3Fe_{0.61}Ni_{0.39}$ in Zr-0.17Fe-0.17Ni alloy [27]
		$a = 0.3324$ $b = 1.0990$ $c = 0.8810$	Zr_3Fe [28]
$Zr_2(Fe_{0.83}Ni_{0.17})$	$a = 0.6461$ $c = 0.5435$	$a = 0.65$ $c = 0.53$	$Zr_2Fe_{0.6}\ Ni_{0.4}$ in Zircaloy-2 [29]
		$a = 0.651$ $c = 0.541$	$Zr_2Fe_{0.5}\ Ni_{0.5}$ in Zircaloy-2 [30]
		$a = 0.66$ $c = 0.55$	$Zr_2Fe_{0.54}Ni_{0.46}$ in Zircaloy-2 [27]
		$a = 0.6385$ $c = 0.5596$	Zr_2Fe [16]
$Zr_{1.02}(Fe_{0.61}Cr_{0.36}Mn_{0.03})_{1.98}$	$a = 0.5034$ $c = 0.8244$	$a = 0.504$ $c = 0.816$	$Zr(Fe_{0.4}Cr_{0.6})_2$ in Zircaloy-2 & 4 [30]
		$a = 0.51$ $c = 0.83$	$Zr(Fe_{0.45}Cr_{0.55})_2$ in Zircaloy-2 [29]
		$a = 0.5019$ $c = 0.8226$	$Zr(Fe_{0.6}Cr_{0.4})_2$ [31]

reported in the literature. The parameters of $Zr(\alpha)$ are slightly larger than those measured in pure zirconium [26]; this may be attributed to the presence of solute elements within the $Zr(\alpha)$ phase.

The Zr_3Fe phase observed in the Zr-8SS alloy exhibits a relatively high solubility for nickel. This high solubility was also observed by Kruger and Adamson in a Zr-0.17Fe-0.17Ni alloy [27]. However, the calculated Fe-Ni-Zr ternary phase diagram [12] suggests that the Zr_3Fe phase has a low Ni solubility, probably because Zr_3Ni does not form in the Ni-Zr binary [32]. In the Zr-8SS alloy, the lattice parameters of $Zr_3(Fe,Ni)$ are similar to those reported for Zr_3Fe [28], except for a slightly larger c parameter. A conclusive determination of nickel influence on Zr_3Fe lattice parameters cannot be made from our data.

The Fe-Zr phase diagram (Fig. 3) indicates that Zr_2Fe is stable only above 775°C. However, Zr_2Ni is known to be a stable compound at room temperature [32]. The Zr_2Ni structure allows for Fe substitution at more than 80% of the Ni sites in the Zr- 8SS alloy. The Fe:Ni ratio in the resulting $Zr_2(Fe,Ni)$ phase is greater the ratios observed for the phase in Zircaloys (see Table VII), probably because of the relatively higher Fe:Ni ratio in the bulk Zr-8SS alloy.

The lattice parameters of $Zr_2(Fe,Ni)$ in the Zr-8SS alloy are comparable to those reported by various investigators [16, 27, 29, 30]. A comparison with Zr_2Fe lattice parameter data indicates that the presence of Ni increases the a parameter and decreases the c parameter of the phase. A similar observation was reported by Havinga *et al*. [16], who studied several pseudo-binary compounds with the $CuAl_2$-type crystal structure.

The lattice parameters of the $ZrFe_2$-$ZrCr_2$ quasi-binary system have been measured by many investigators [13–15, 29–31]. Both $ZrFe_2$ and $ZrCr_2$ have the C15 (cubic) structure, but $Zr(Fe_xCr_{1-x})_2$ alloys with $0.1 \leq x \leq 0.8$ have the C14 (hexagonal) crystal structure. Increasing the chromium content of the $Zr(Fe_xCr_{1-x})_2$ alloys increases both the a and c lattice parameters of the C14 structure. The measured lattice parameters of the C14 intermetallic in the Zr-8SS alloy are generally in agreement with values reported in the literature.

5. Summary

The microstructures of as-cast and thermally aged Zr-8SS alloys were studied by neutron diffraction, scanning electron microscopy, and energy dispersive spectroscopy. The phases observed in as-cast alloys were the solid-solution phase $Zr(\alpha)$ and the intermetallic phases $Zr_3(Fe,Ni)$, $Zr_3(Fe,Cr)$, $Zr_2(Fe,Ni)$, $Zr_2(Fe,Cr)$, and $Zr(Fe,Cr)_2$. Thermal aging at 780°C for 30 days resulted in an increase in $Zr_3(Fe,Ni)$ and a decrease in $Zr_2(Fe,Ni)$ phase content. The non-equilibrium phases, $Zr_3(Fe,Cr)$ and $Zr_2(Fe,Cr)$, were absent in the aged sample. The measured phase lattice parameters were comparable to those reported for similar phases in the literature. A solidification sequence has been proposed to explain the as-cast alloy phases, and mechanisms have been proposed to explain the phase changes observed during thermal aging.

Acknowledgments

The authors acknowledge L. Leibowitz for reviewing the manuscript and for helpful discussions. The work was supported by the U.S. Dept. of Energy under contract W-31-109-Eng-38. This work has benefited from the use of the Intense Pulsed Neutron Source at Argonne National Laboratory. This facility is funded by the U.S. Department of Energy, BES-Materials Science, under contract W-31-109-ENG-38.

References

1. C. C. McPHEETERS, E. C. GAY, E. J. KARELL and J. P. ACKERMAN, *JOM* **49** (1997) 22.
2. S. M. McDEAVITT, D. P. ABRAHAM and J. Y. PARK, *J. Nucl. Mater.* **257** (1998) 21.

3. B. COX, "Advances in Corrosion Science and Technology," Vol. 5 (Plenum Press, New York, 1976) p. 173.
4. S. KASS, Corrosion of Zirconium Alloys, ASTM STP-368, American Society for Testing of Materials, Philadelphia, PA, 1964, p. 3.
5. D. ARIAS, M. S. GRANOVSKY and J. P. ABRIATA, "Phase Diagrams of Binary Iron Alloys," edited by H. Okamoto (ASM International, Materials Park, OH, 1993) p. 467.
6. D. ARIAS and J. P. ABRIATA, "Binary Alloy Phase Diagrams," Vol. 2, edited by T. P. MASSALSKI (ASM International, Materials Park, OH, 1990) p. 1798.
7. D. P. ABRAHAM, Argonne National Laboratory, unpublished data.
8. A. C. LARSON and R. B. VON DREELE, Los Alamos National Laboratory Report, LAUR 86-748, 1986.
9. J. P. ABRIATA, J. GARCES and R. VERSACI, *Bull. Alloy Phase Diagrams* **7** (1986) 116.
10. B. O. LICHTER, *Trans. Metall. Soc. AIME* **218** (1960) 1015.
11. V. RAGHAVAN, "Phase Diagrams of Ternary Iron Alloys, Part 6B" (Indian Institute of Metals, Calcutta, 1992) p. 711.
12. *Idem.* "Phase Diagrams of Ternary Iron Alloys, Part 6B" (Indian Institute of Metals, Calcutta, 1992) p. 1094.
13. S. C. MOSS, Ph.D. Thesis, Massachusetts Inst. Technol., Cambridge, MA, 1959.
14. K. KANEMATSU and Y. FUJITA, *J. Phys. Soc. Japan* **29** (1970) 864.
15. D. SHALTIEL, I. JACOB and D. DAVIDOV, *J. Less-Common Metals* **53** (1977) 117.
16. E. E. HAVINGA, H. DAMSMA and P. HOKKELING, *ibid.* **27** (1972) 169.
17. D. ARIAS and J. P. ABRIATA, *Bull. Alloy Phase Diagrams* **7** (1986) 237.
18. J. A. SAWICKI, G. M. HOOD, H. ZOU and R. J. SCHULTZ, *J. Nucl. Mater.* **218** (1995) 161.
19. R. A. HOLT, *ibid.* **35** (1970) 322.
20. G. OKVIST and K. KALLSTROM, *ibid.* **35** (1970) 316.
21. J. CREPIN, T. BRETHEAU, D. CALDEMAISON, A. BARBU and G. JAZKIEROWITCZ, *J. Mater. Sci.* **32** (1997) 4841.
22. J. CREPIN, T. BRETHEAU and D. CALDEMAISON, *Acta Metall. Mater.* **43** (1995) 3709.
23. N. RAO and V. BANGARU, *J. Nucl. Mater.* **131** (1985) 280.
24. T. E. PEREZ and M. E. SAGESSE, *Metallography* **15** (1982) 43.
25. D. A. PORTER and K. E. EASTERLING, "Phase Transformations in Metals and Alloys" (Van Nostrand Reinhold International, Berkshire, England, 1981) p. 314.
26. J. GOLDAK, L. T. LLOYD and C. S. BARRETT, *Phys. Rev.* **144** (1966) 478.
27. R. M. KRUGER and R. B. ADAMSON, *J. Nucl. Mater.* **205** (1993) 242.
28. K. H. J. BUSCHOW, *J. Less-Common Metals* **79** (1981) 243.
29. P. CHEMELLE, D. B. KNORR, J. B. VAN DER SANDE and R. M. PELLOUX, *J. Nucl. Mater.* **113** (1983) 58.
30. W. J. S. YANG, R. P. TUCKER, B. CHENG and R. B. ADAMSON, *ibid.* **138** (1986) 185.
31. O. CANET, M. LATROCHE, F. BOURÉE-VIGNERON and A. PERCHERON-GUÉGAN, *J. Alloys Comp.* **210** (1994) 129.
32. P. NASH and C. S. JAYANATH, *Bull. Alloy Phase Diagrams* **5** (1984) 144.

Received 24 October 2000
and accepted 25 July 2001